

Supporting Information

BiFeO₃-Based Flexible Ferroelectric Memristors for Neuromorphic Pattern Recognition

*Haoyang Sun,^{†,‡} Zhen Luo,^{†,‡} Letian Zhao,[†] Chuanchuan Liu,[†] Chao Ma,[†] Yue Lin,[†]
Guanyin Gao,[†] Zhiwei Chen,[†] Zhiwei Bao,[†] Xi Jin,[†] Yuewei Yin,^{*} Xiaoguang Li^{*,†,§}*

[†] Hefei National Laboratory for Physical Sciences at the Microscale, Department of Physics, and CAS key Laboratory of Strongly-Coupled Quantum Matter Physics, University of Science and Technology of China, Hefei 230026, China

[§] Collaborative Innovation Center of Advanced Microstructures, Nanjing 210093, China

[‡] Haoyang Sun and Zhen Luo contributed equally to this work.

Corresponding Authors

*Email: lixg@ustc.edu.cn (X.G.L.)

*Email: yyw@ustc.edu.cn (Y.W.Y.)

- S1. Surface morphology of the mica substrate and transparency characterizations
- S2. XRD θ - 2θ scan patterns around BFO (121), (221), and (131) peaks
- S3. Reciprocal space mapping, XRD ϕ scan patterns and the schematic diagram of the epitaxial structure of BFO/SRO/BTO/mica
- S4. Ferroelectric displacements of Fe and O ions
- S5. Comparison of the ferroelectric polarizations among various flexible ferroelectric films
- S6. PFM measurements of the flexible BFO thin film
- S7. Schematic of pulse sequence for the R - V_p loop
- S8. I - V loop of the Au/BFO/SRO/BTO/mica flexible memristor
- S9. Artificial neural network simulation
- S10. Schematic of bending tests

S1. Surface morphology of the mica substrate and transparency characterizations

The surface morphology of the mica substrate was probed by an atomic force microscope (AFM). As shown in Figure S1a, the mica substrate exhibits an ultra-smooth surface with a root mean square roughness $R_{\text{rms}} \sim 11$ pm. Figure S1b illustrates the transmittance spectra measured by an ultraviolet-visible spectroscopy. It can be seen that the transmittance of a mica substrate is over 90% in the range of the visible light. The transmittance of SRO/BTO/mica and BFO/SRO/BTO/mica samples are near 50% in the wavelength range of 500-750 nm, demonstrating their semitransparency property.

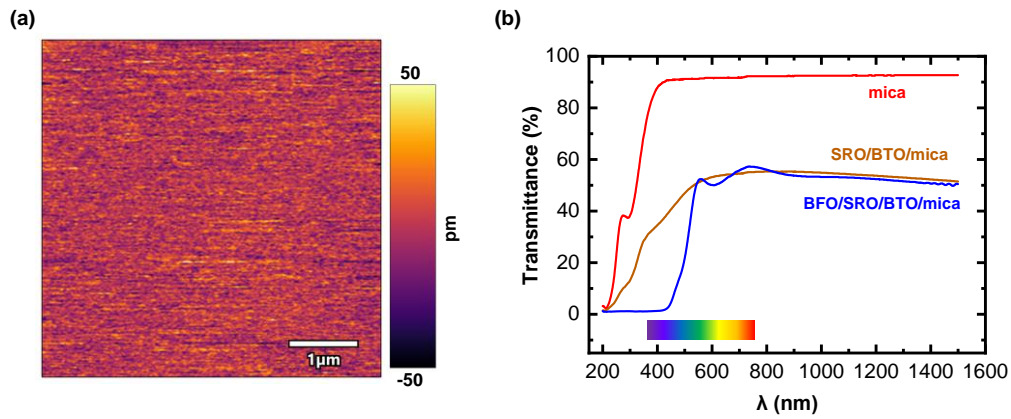


Figure S1. (a) AFM topography image of a mica substrate in a $5 \times 5 \mu\text{m}^2$ region. (b) Transmittances of mica, SRO/BTO/mica and BFO/SRO/BTO/mica. The inset color bar indicates the wavelength range of the visible light.

S2. XRD θ - 2θ scan patterns around BFO (121), (221), and (131) peaks

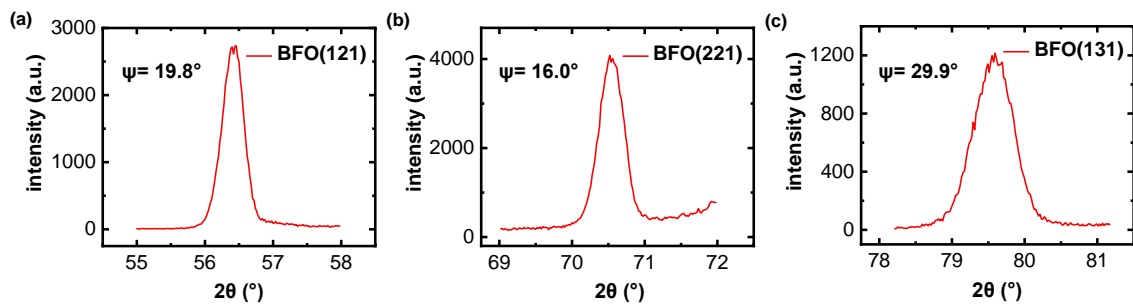


Figure S2. XRD θ - 2θ scan patterns around (a) BFO (121), (b) BFO (221) and (c) BFO (131) peaks.

Figures S2a-c show the XRD θ - 2θ scan patterns around BFO (121), (221), and (131) peaks measured at different inclination angles ψ of $\sim 19.8^\circ$, $\sim 16.0^\circ$ and $\sim 29.9^\circ$, respectively. Combining with the result of XRD θ - 2θ scan pattern in Figure 1a of the main text, the lattice parameters for BFO are estimated as $a = b = c \sim 3.951 \text{ \AA}$, $\alpha \sim 89.3^\circ$.

S3. Reciprocal space mapping, XRD ϕ scan patterns and the schematic diagram of the epitaxial structure of BFO/SRO/BTO/mica

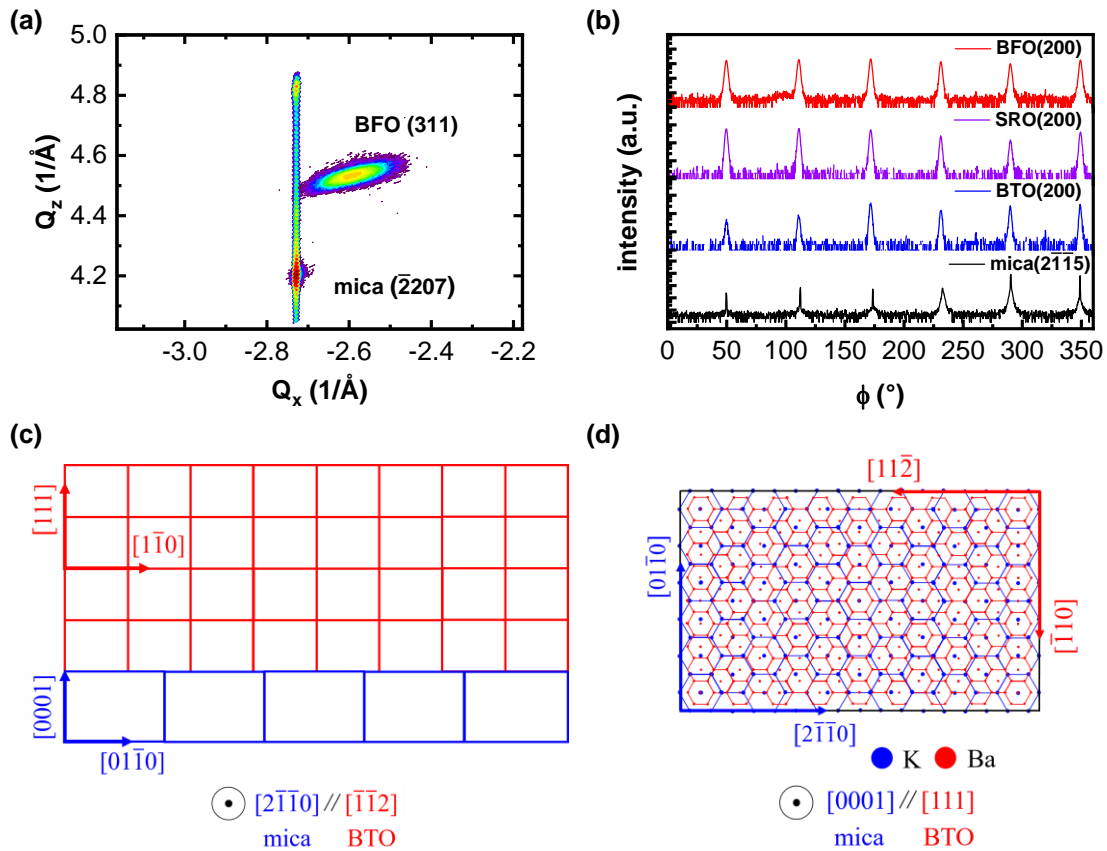


Figure S3. (a) Reciprocal space mapping around the mica ($\bar{2}207$) and BFO (311) diffraction peaks. (b) XRD ϕ scan patterns for BFO (200), SRO (200), BTO (200) and mica ($2\bar{1}15$) diffraction peaks. (c, d) Schematic of the epitaxial relationship between (0001)-oriented mica substrate (blue) and the (111)-oriented BTO buffer layer (red). (c) Side view with the $[2\bar{1}\bar{1}0]$ zone axis of mica or $[\bar{1}\bar{1}2]$ zone axis of BTO. (d) Top view of the (0001) surface of mica and the (111) surface of BTO.

To reveal the detailed structural information, the reciprocal space mapping (RSM)¹ around BFO (311) and mica ($\bar{2}207$) peaks was investigated, as shown in Figure S3a, confirming the good hetero-epitaxial growth of the BFO-based heterostructure. As shown in Figure S3b, XRD ϕ scan patterns of BFO, SRO, BTO and mica were characterized to analyze the in-plane epitaxial relationship of the heterostructure. The XRD ϕ scan patterns at $(200)_{\text{BFO}}$, $(200)_{\text{SRO}}$, $(200)_{\text{BTO}}$ and $(2\bar{1}15)_{\text{mica}}$ exhibit multiple peaks at 60° intervals, indicating a six-fold symmetry. In Figure S3c, the schematic of the BTO buffer layer grown

on the mica substrate along the zone axis of mica $[2\bar{1}\bar{1}0]$ is shown, and Figure S3d shows the top view of the interface between BTO and mica along the zone axis of mica $[0001]$. The similar pseudo-hexagonal configuration between the surface structures of mica and BTO can make them nest in a periodic way, which reveals an epitaxial relationship of $(111)_{\text{BTO}}//(\text{0001})_{\text{mica}}$ and $[\bar{1}\bar{1}0]_{\text{BTO}}//[0\bar{1}\bar{1}0]_{\text{mica}}$. Therefore, combining with the result of XRD θ - 2θ scan pattern in Figure 1a of the main text, the out-of-plane and in-plane epitaxial relationships can be determined as $(111)_{\text{BFO}}//(\text{111})_{\text{SRO}}//(\text{111})_{\text{BTO}}//(\text{0001})_{\text{mica}}$ and $[\bar{1}\bar{1}0]_{\text{BFO}}//[\bar{1}\bar{1}0]_{\text{SRO}}//[\bar{1}\bar{1}0]_{\text{BTO}}//[0\bar{1}\bar{1}0]_{\text{mica}}$, respectively.

Based on the in-plane epitaxial relationship and the growth sequence of the BFO/SRO/BTO/mica heterostructure, the lattice mismatches between different materials can be calculated using their bulk lattice parameters, as shown in Table S1. It can be seen that the lattice mismatch between BTO and mica ($\sim 1.49\%$) or between SRO and BTO ($\sim 1.75\%$) is much smaller than that between SRO and mica ($\sim 3.33\%$), and this makes BTO as a good buffer layer for the subsequent film growths. Especially, the mismatch between BFO and SRO is even smaller (-0.76%). As a result, the utilization of the SRO/BTO buffer layers will lower the mismatch strain on BFO and improve its epitaxial quality.

Table S1. Lattice mismatches among BFO, SRO, BTO, and mica according to the growth sequence of the BFO/SRO/BTO/mica heterostructure, calculated using their bulk lattice parameters

Perovskite film		BTO	SRO	BFO
Bulk lattice parameter		$\sim 4.00 \text{ \AA}$	$\sim 3.93 \text{ \AA}$	$\sim 3.96 \text{ \AA}$
Lattice mismatch	on mica	+1.49%	+3.33%	+2.85%
	on BTO	—	+1.75%	+1.00%
	on SRO	—	—	-0.76%

+: Tensile in-plane strain; -: Compressive in-plane strain

S4. Ferroelectric displacements of Fe and O ions

Table S2 summaries the Fe and O ion average displacements projected along the $[111]$ and $[2\bar{1}\bar{1}]$ directions, which were estimated from the aberration-corrected high-angle annular dark-field scanning transmission electron microscopy (HAADF-STEM) and

annular bright field (ABF) STEM images in Figure 1g and h. It should be pointed out that the very small displacements along $[2\bar{1}\bar{1}]$ direction are almost within the technical precision (about several picometers) of STEM measurements.²

Table S2. Fe and O ion average displacements projected in $(0\bar{1}\bar{1})$ plane

	Displacement along $[111]$ direction	Displacement along $[2\bar{1}\bar{1}]$ direction
Fe shift in HAADF	-38.7 pm	-2.1 pm
Fe shift in ABF	-38.2 pm	-1.8 pm
O shift in ABF	-68.2 pm	-7.8 pm

S5. Comparison of the ferroelectric polarizations among various flexible ferroelectric films

Figure S4 summarizes the saturated polarization (P_s) and remnant polarization (P_r) for various flexible ferroelectric films.³⁻¹⁷ The Au/BFO/SRO/BTO/mica flexible heterostructure in our work shows the infusive results with the highest P_s and P_r among all the reported flexible ferroelectric films at present.

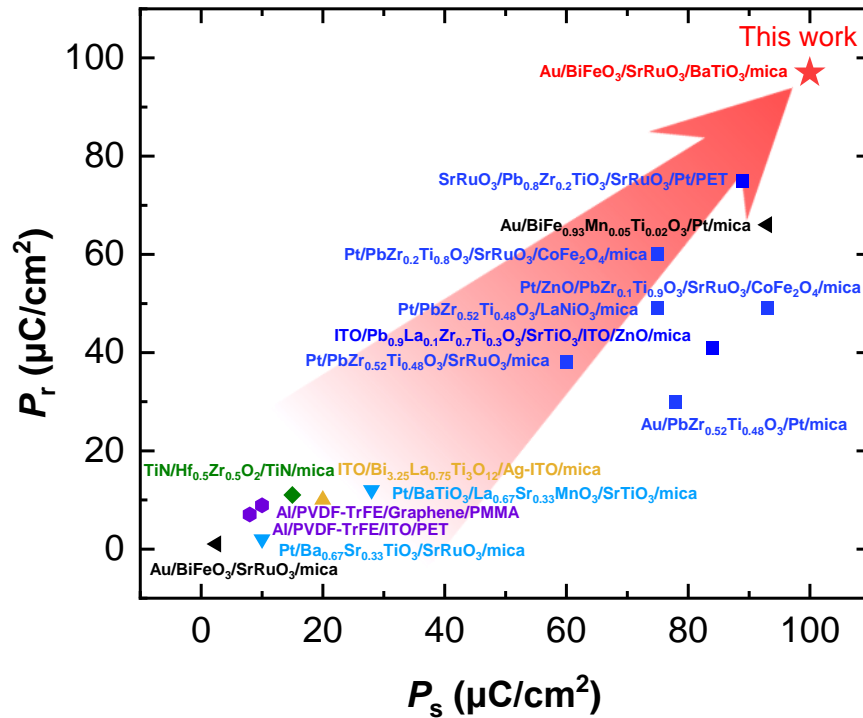


Figure S4. Comparison of the saturated polarization (P_s) and remnant polarization (P_r) of various flexible ferroelectric devices.³⁻¹⁷

S6. PFM measurements of the flexible BFO thin film

The surface morphology of BFO thin film measured by AFM over an area of $5 \times 5 \mu\text{m}^2$ is shown in Figure S5a. The RMS roughness is $\sim 12.6 \text{ nm}$. Figure S5b shows the piezoresponse force microscopy (PFM) phase and amplitude hysteresis loops measured on the bare surface of BFO. The square loop with a 180° change in PFM phase and the typical butterfly-like loop in PFM amplitude demonstrate the switchable ferroelectricity in the BFO thin film. Figure S5c shows the image of PFM phase after the box-in-box switched patterns poled at $\pm 20 \text{ V}$. The PFM tip bias of $+20 \text{ V}$ is used to pole the $3 \times 3 \mu\text{m}^2$ square region, and subsequently the center of $1 \times 1 \mu\text{m}^2$ square area is poled by -20 V . The PFM phase image shows a 180° dark and bright contrast corresponding to the downward and upward polarizations, respectively, demonstrating the switchable ferroelectric domains in BFO. Furthermore, the contrast of the area outside of the $3 \times 3 \mu\text{m}^2$ square region is similar to the center $1 \times 1 \mu\text{m}^2$ region, demonstrating that the spontaneous polarization of an as-grown BFO thin film is upward.

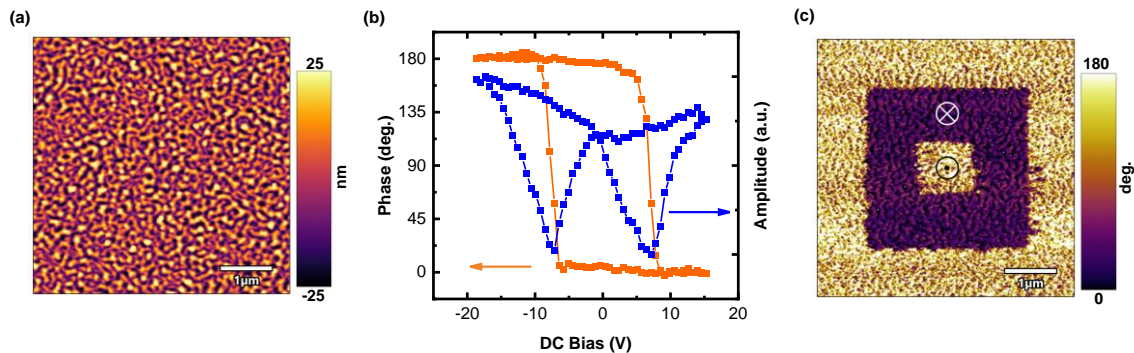


Figure S5. (a) AFM topography image of BFO film in a $5 \times 5 \mu\text{m}^2$ region. (b) PFM hysteresis loops. The orange curve represents the PFM phase signal, and the blue curve represents the PFM amplitude signal. (c) PFM phase image recorded after writing an area of $3 \times 3 \mu\text{m}^2$ with $+20 \text{ V}$ and the central $1 \times 1 \mu\text{m}^2$ with -20 V by a biased conductive tip.

S7. Schematic of pulse sequence for the R - V_p loop

To investigate the memristive behaviors, the resistance (read voltage $V_r = +2 \text{ V}$) versus pulse voltage (V_p) loops were carried out. Figure S6 shows the voltage pulse sequence for the R - V_p measurement.

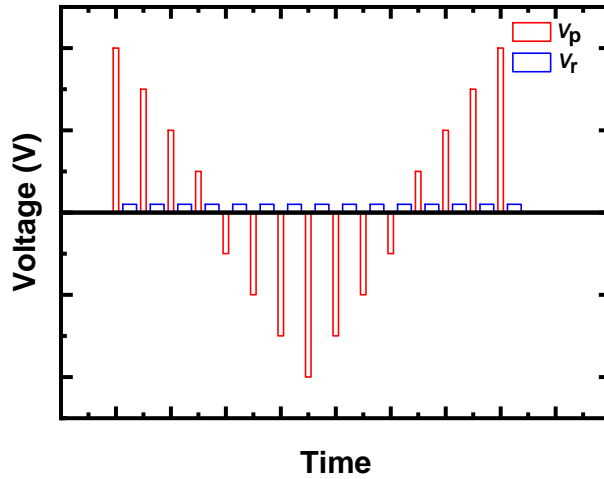


Figure S6. Applied voltage pulse sequence for R - V_p loop.

S8. I - V loop of the Au/BFO/SRO/BTO/mica flexible memristor

Figure S7 shows a typical I - V loop of the Au/BFO/SRO/BTO/mica flexible memristor. By sweeping the voltage in a sequence of $0\text{ V} \rightarrow 8\text{ V} \rightarrow -8\text{ V} \rightarrow 0\text{ V}$, the typical pinched I - V loop indicates the memristive characteristic, similar to earlier reports.^{18,19} In addition, the hysteresis I - V loop suggests a bipolar resistance switching behavior, which is commonly observed in previous ferroelectric heterostructures grown on rigid substrates and should be related to the ferroelectricity tuned interface barrier.²⁰

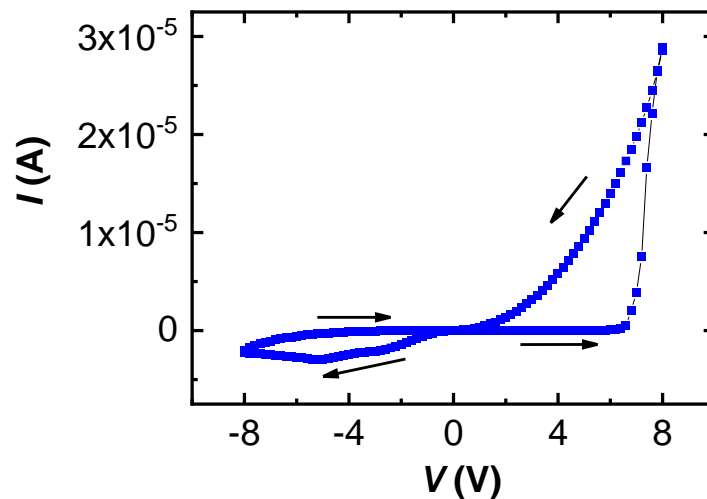


Figure S7. Typical I - V loop of the Au/BFO/SRO/BTO/mica flexible memristor measured by sweeping voltage in the sequence of $0\text{ V} \rightarrow 8\text{ V} \rightarrow -8\text{ V} \rightarrow 0\text{ V}$. The arrows indicate the direction of voltage sweeping.

S9. Artificial neural network simulation

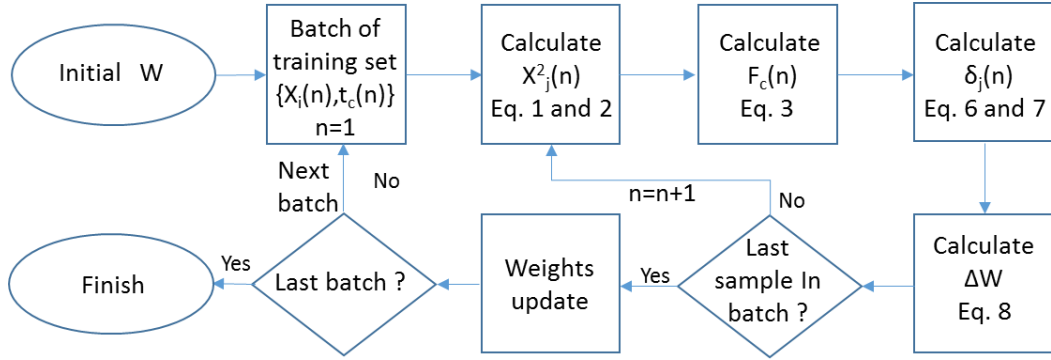


Figure S8. Flow chart of the training process.

To recognize Modified National Institute Standard and Technology (MNIST) handwritten digits through an online supervised learning, a two-layer perceptron neural network with 784 input neurons (corresponding to a 28×28 pixels MNIST image), 100 hidden neurons, and 10 output neurons (corresponding to 10 classes of digit (0 - 9)) was simulated, as shown in Figure 6c in the main text. According to the back propagation (BP) algorithm for a deep neural network (DNN), the learning process is composed of two stages: the feedforward inference and the feedback weight update,²¹ as the flow chart illustrated in Figure S8.

For each training cycle, 128 images randomly selected from 60000 MNIST digits are set as a batch. The input vector $X^1(n)$ to the first layer corresponds to a set of small reading voltages whose amplitudes encode an image from the training dataset,²¹ and the indicator n (1~128) is the number of image in each batch. Based on the output vector of the first layer (I^1), the input vector $X^2(n)$ and the output vector $F_c(n)$ for the second layer are obtained by using eqs 1-3.²¹

$$I_j^l = \sum_i W_{ij}^l X_i^l . \quad (1)$$

$$X_j^2 = a[\text{ReLU} (I_j^1)]. \quad (2)$$

$$F_c(n) = \text{softmax}(\sum_{j=1}^{100} W_{cj}^2 X_j^2). \quad (3)$$

Here, l is the layer number, and W^l is the weight matrix of the corresponding layer. a scales the output of the first layer to the input of the second layer.²¹ The *ReLU* function is the activation function defined as:

$$\text{ReLU}(x) = \max(0, x) . \quad (4)$$

The softmax function in eq 3 is defined as:

$$y_c(n) = \frac{e^{ml_c(n)}}{\sum_{p=1}^{10} e^{ml_p(n)}}, \quad (5)$$

where $y_c(n)$ is the probability that Image n belongs to Class c . Then, to evaluate the difference between the calculated output $F_c(n)$ and ideal result possibility $t_c(n)$, the cross-entropy loss function $\xi(n)$ was calculated by using eq 6:

$$\xi(T(n), F(n)) = -\sum_{c=1}^{10} t_c(n) \log[F_c(n)]. \quad (6)$$

As for the feedback weight update process, the desired weight updates (ΔW) of synaptic devices in each layer were calculated by using eqs 7 and 8:

$$\delta_j^l = \begin{cases} \frac{\partial \xi}{\partial I_j^l}, & l = 2; \\ \frac{\partial \sigma}{\partial I_j^l} \sum_i W_{ij}^l \delta_i^{l+1}, & l = 1. \end{cases} \quad (7)$$

$$\Delta W^l = \eta \sum_{n=1}^B \frac{\delta^l(n) X^l(n)^T}{B}. \quad (8)$$

Here, σ is the nonlinear activation function of the hidden layer, and the learning rate η is obtained from the BP algorithm.

For our simulations, the DNN synaptic weight of the memristor crossbar is encoded as the conductance (G) difference between two memristors:²¹

$$W_{ij}^l = G_{ij}^{l+} - G_{ij}^{l-}. \quad (9)$$

Namely, each synapse in the DNN is implemented by two memristors, so that the total number of memristors in the crossbar is $(784 \times 100 + 100 \times 10) \times 2 = 158800$. Here, the weight update is performed by software but based on the realistic device performances.

S10. Schematic of bending tests

Figure S9 shows the schematic of the bending tests for the Au/BFO/SRO/BTO/mica flexible memristor. The bending induced strain on the thin film can be approximately calculated through:²²

$$\varepsilon = (t_{\text{film}} + t_{\text{mica}}) / 2r, \quad (10)$$

where t_{film} and t_{mica} are the thicknesses of the film and the mica substrate, respectively. The bending radius r of the flexible heterostructure can be calculated by the following

formula:²²

$$r = L / \left(2\pi \sqrt{\frac{dL}{L} - \frac{\pi^2 (t_{\text{film}} + t_{\text{mica}})^2}{12L^2}} \right), \quad (11)$$

where L denotes the length of the heterostructure along the bending direction and dL represents the length variation along the bending direction. In this work, the strain ε is defined as positive for the tensile strain and as negative for the compressive strain.

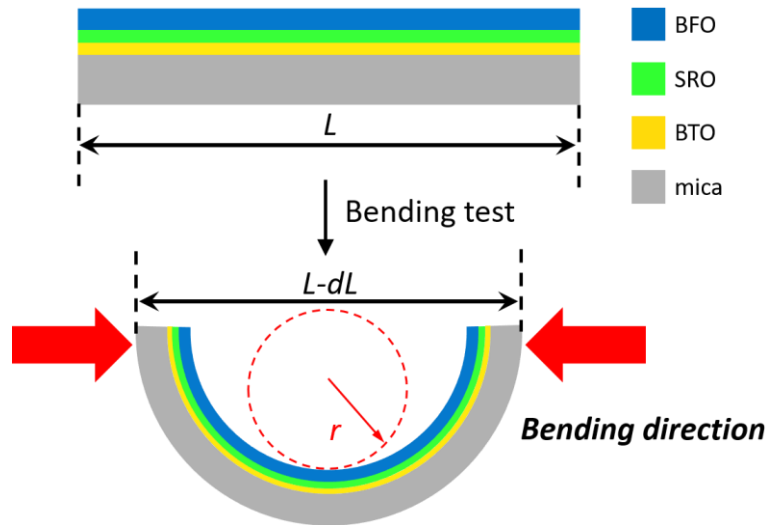


Figure S9. Schematic of bending tests of the Au/BFO/SRO/BTO/mica flexible memristor. Top panel: device under flat condition. Lower panel: device under bending condition.

REFERENCES

- (1) Fewster, P. F. Reciprocal Space Mapping. *Crit. Rev. Solid State Mater. Sci.* **1997**, *22*, 69-110.
- (2) Yankovich, A. B.; Berkels, B.; Dahmen, W.; Binev, P.; Sanchez, S. I.; Bradley, S. A.; Li, A.; Szlufarska, I.; Voyles, P. M. Picometre-Precision Analysis of Scanning Transmission Electron Microscopy Images of Platinum Nanocatalysts. *Nat. Commun.* **2014**, *5*, 4155.
- (3) Jiang, J.; Bitla, Y.; Huang, C. W.; Do, T. H.; Liu, H. J.; Hsieh, Y. H.; Ma, C. H.; Jang, C. Y.; Lai, Y. H.; Chiu, P. W.; Wu, W. W.; Chen, Y. C.; Zhou, Y. C.; Chu, Y. H. Flexible Ferroelectric Element Based on van der Waals Heteroepitaxy. *Sci. Adv.* **2017**, *3*, e1700121.
- (4) Gao, W. X.; You, L.; Wang, Y. J.; Yuan, G. L.; Chu, Y. H.; Liu, Z. G.; Liu, J. M. Flexible $\text{PbZr}_{0.52}\text{Ti}_{0.48}\text{O}_3$ Capacitors with Giant Piezoelectric Response and Dielectric Tunability. *Adv. Electron. Mater.* **2017**, *3*, 1600542.
- (5) Wang, D.; Yuan, G. L.; Hao, G. Q.; Wang, Y. J. All-Inorganic Flexible Piezoelectric

- Energy Harvester Enabled by Two-Dimensional Mica. *Nano Energy* **2018**, *43*, 351-358.
- (6) Ma, C. H.; Jiang, J.; Shao, P. W.; Peng, Q. X.; Huang, C. W.; Wu, P. C.; Lee, J. T.; Lai, Y. H.; Tsai, D. P.; Wu, J. M.; Lo, S. C.; Wu, W. W.; Zhou, Y. C.; Chiu, P. W.; Chu, Y. H. Transparent Antiradiative Ferroelectric Heterostructure Based on Flexible Oxide Heteroepitaxy. *ACS Appl. Mater. Interfaces* **2018**, *10*, 30574-30580.
- (7) Gao, D.; Tan, Z. W.; Fan, Z.; Guo, M.; Hou, Z. P.; Chen, D. Y.; Qin, M. H.; Zeng, M.; Zhou, G. F.; Gao, X. S.; Lu, X. B.; Liu, J. M. All-Inorganic Flexible Ba_{0.67}Sr_{0.33}TiO₃ Thin Films with Excellent Dielectric Properties over a Wide Range of Frequencies. *ACS Appl. Mater. Interfaces* **2019**, *11*, 27088-27097.
- (8) Gao, H.; Yang, Y. X.; Wang, Y. J.; Chen, L.; Wang, J. L.; Yuan, G. L.; Liu, J. M. Transparent, Flexible, Fatigue-Free, Optical-Read, and Nonvolatile Ferroelectric Memories. *ACS Appl. Mater. Interfaces* **2019**, *11*, 35169-35176.
- (9) Yang, C. H.; Han, Y. J.; Qian, J.; Lv, P. P.; Lin, X. J.; Huang, S. F.; Cheng, Z. X. Flexible, Temperature-Resistant, and Fatigue-Free Ferroelectric Memory Based on Bi(Fe_{0.93}Mn_{0.05}Ti_{0.02})O₃ Thin Film. *ACS Appl. Mater. Interfaces* **2019**, *11*, 12647-12655.
- (10) Wu, J. Y.; Liang, Z. S.; Ma, C. R.; Hu, G. L.; Shen, L. K.; Sun, Z. X.; Zhang, Y.; Lu, L.; Liu, M.; Jia, C. L. Flexible Lead-Free BaTiO₃ Ferroelectric Elements with High Performance. *IEEE Electron Device Lett.* **2019**, *40*, 889-892.
- (11) Xiao, W. W.; Liu, C.; Peng, Y.; Zheng, S. Z.; Feng, Q.; Zhang, C. F.; Zhang, J. C.; Hao, Y.; Liao, M.; Zhou, Y. C. Thermally Stable and Radiation Hard Ferroelectric Hf_{0.5}Zr_{0.5}O₂ Thin Films on Muscovite Mica for Flexible Nonvolatile Memory Applications. *ACS Appl. Electron. Mater.* **2019**, *1*, 919-927.
- (12) Kim, K. L.; Lee, W.; Hwang, S. K.; Joo, S. H.; Cho, S. M.; Song, G.; Cho, S. H.; Jeong, B.; Hwang, I.; Ahn, J. H.; Yu, Y. J.; Shin, T. J.; Kwak, S. K.; Kang, S. J.; Park, C. Epitaxial Growth of Thin Ferroelectric Polymer Films on Graphene Layer for Fully Transparent and Flexible Nonvolatile Memory. *Nano Lett.* **2016**, *16*, 334-340.
- (13) Singh, D.; Deepak; Garg, A. An Efficient Route to Fabricate Fatigue-Free P(VDF-TrFE) capacitors with Enhanced Piezoelectric and Ferroelectric Properties and Excellent Thermal Stability for Sensing and Memory Applications. *Phys. Chem. Chem. Phys.* **2017**, *19*, 7743-7750.
- (14) Bakaul, S. R.; Serrao, C. R.; Lee, O.; Lu, Z. Y.; Yadav, A.; Carraro, C.; Maboudian, R.; Ramesh, R.; Salahuddin, S. High Speed Epitaxial Perovskite Memory on Flexible Substrates. *Adv. Mater.* **2017**, *29*, 1605699.
- (15) Yang, C. H.; Han, Y. J.; Qian, J.; Cheng, Z. X. Flexible, Temperature-Stable, and

Fatigue-Endurable $\text{PbZr}_{0.52}\text{Ti}_{0.48}\text{O}_3$ Ferroelectric Film for Nonvolatile Memory. *Adv. Electron. Mater.* **2019**, *5*, 1900443.

(16)Ren, C. L.; Zhong, G. K.; Xiao, Q.; Tan, C. B.; Feng, M.; Zhong, X. L.; An, F.; Wang, J. B.; Zi, M. F.; Tang, M. K.; Tang, Y.; Jia, T. T.; Li, J. Y. Highly Robust Flexible Ferroelectric Field Effect Transistors Operable at High Temperature with Low - Power Consumption. *Adv. Funct. Mater.* **2020**, *30*, 1906131.

(17)Xie, Z. S.; Yang, Y. X.; Fang, L.; Wang, Y. J.; Ding, X. F.; Yuan, G. L.; Liu, J. M. Photovoltaic, Photo-Impedance, and Photo-Capacitance Effects of the Flexible (111) BiFeO_3 Film. *Appl. Phys. Lett.* **2019**, *115*, 112902.

(18)Lin, Y. B.; Yan, Z. B.; Lu, X. B.; Lu, Z. X.; Zeng, M.; Chen, Y.; Gao, X. S.; Wan, J. G.; Dai, J. Y.; Liu, J. M. Temperature-Dependent and Polarization-Tuned Resistive Switching in $\text{Au/BiFeO}_3/\text{SrRuO}_3$ Junctions. *Appl. Phys. Lett.* **2014**, *104*, 143503.

(19)Hong, S.; Choi, T.; Jeon, J. H.; Kim, Y.; Lee, H.; Joo, H. Y.; Hwang, I.; Kim, J. S.; Kang, S. O.; Kalinin, S. V.; Park, B. H. Large Resistive Switching in Ferroelectric BiFeO_3 Nano-Island Based Switchable Diodes. *Adv. Mater.* **2013**, *25*, 2339-2343.

(20)Jiang, A. Q.; Wang, C.; Jin, K. J.; Liu, X. B.; Scott, J. F.; Hwang, C. S.; Tang, T. A.; Lu, H. B.; Yang, G. Z. A Resistive Memory in Semiconducting BiFeO_3 Thin-Film Capacitors. *Adv. Mater.* **2011**, *23*, 1277-1281.

(21)Li, C.; Belkin, D.; Li, Y. N.; Yan, P.; Hu, M.; Ge, N.; Jiang, H.; Montgomery, E.; Lin, P.; Wang, Z. R.; Song, W. H.; Strachan, J. P.; Barnell, M.; Wu, Q.; Williams, R. S.; Yang, J. J.; Xia, Q. F. Efficient and Self-Adaptive In-situ Learning in Multilayer Memristor Neural Networks. *Nat. Commun.* **2018**, *9*, 2385.

(22)Mao, L. J.; Meng, Q. H.; Ahmad, A.; Wei, Z. X. Mechanical Analyses and Structural Design Requirements for Flexible Energy Storage Devices. *Adv. Energy Mater.* **2017**, *7*, 1700535.